

# Enigmatic doubly scattered tube waves at a crosswell seismic survey

Nori Nakata<sup>1,2</sup>, Rie Nakata<sup>1,3</sup>, Ayato Kato<sup>4</sup>, Ziqiu Xue<sup>5</sup>, and Malcolm C. A. White<sup>2</sup>

<sup>1</sup> Lawrence Berkeley National Laboratory, Berkeley, USA

<sup>2</sup> Massachusetts Institute of Technology, Cambridge, USA

<sup>3</sup> University of Tokyo, Tokyo, Japan

<sup>4</sup> Japan Oil, Gas and Metals National Corporation, Tokyo, Japan

<sup>5</sup> Research Institute of Innovative Technology for the Earth, Kyoto, Japan

22 November 2022

## SUMMARY

Enigmatically strong tube waves continue to exist long after the direct wave during repeat crosswell-monitoring surveys at the Nagaoka CO<sub>2</sub> injection site in Japan. The tube waves, which have linear moveouts with velocities of 1.29 and 1.41 km/s at plastic and steel casings, respectively, are generated by double scattering on the shallow side of the wells. We characterize wavefields to confirm that these late coda waves are tube waves that are excited at the source well, propagate upward, then travel to a receiver well as a body wave, and finally propagate downward along the receiver well. Even though these tube waves result from second-order scattering, they have large amplitudes because of the relatively short distance between source and receiver wells. Because these waves propagate along both wells many times, we can extract detailed information of wave propagation by averaging them to increase the signal-to-noise ratio. We first use the tube waves to relocate sources and receivers between multiple monitoring surveys, demonstrating our ability to correct the severe noise caused by location errors that frequently degrades the repeatability of time-lapse surveys. Then we apply an inversion based on the physics of tube waves to estimate the location and strength of the scatterers and find that

they are predominantly located in the shallow segment of the wells, above the sources, and infer that they are related to local fractures and/or wellbore conditions because their locations do not correspond to the well geometry. Lastly, we use the tube waves to accurately estimate subsurface velocities along the wells. The estimation is stable and robust, and the velocities follow the general trend of subsurface structure seen in the well log data. Due to the receiver spacing, tube-wave analysis cannot resolve a thin, high-velocity layer at the CO<sub>2</sub> reservoir. By combining tube waves observed during different stages of the monitoring survey, we can estimate the time-lapse changes of the subsurface velocities.

**Keywords:** Guided waves, Wave propagation, Wave scattering and diffraction, Time series analysis, Tube waves, Crosshole

## 1 INTRODUCTION

Tube waves are frequently observed to be one of the most energetic wave phases during bore-hole seismic surveys, especially Vertical Seismic Profiling (VSP) surveys, and are often treated as strong coherent noise because they mask weaker body waves (Herman *et al.*, 2000). Tube waves contain information pertaining to wellbore characteristics (Biot, 1952; Cheng & Toksöz, 1981; Meredith *et al.*, 1993) and subsurface fractures that intersect the wells (Tezuka *et al.*, 1997; Bakku *et al.*, 2013; Minato *et al.*, 2017; Zheng *et al.*, 2018). Because tube waves are Stoneley waves, they can also be used to constrain permeability parameters (Li *et al.*, 1994), which are usually difficult parameters to estimate from seismic data alone.

We observed unusually strong tube waves during repeating crosswell seismic surveys in 2003–2005 at Nagaoka, Japan. The crosswell surveys were designed for monitoring CO<sub>2</sub> injection using seismic tomography (Saito *et al.*, 2006). Geological CO<sub>2</sub> sequestration is becoming increasingly critical to achieving negative emission objectives (Bickle, 2009), and seismic tomography and crosswell seismic surveys are useful tools for monitoring CO<sub>2</sub> plume behaviour. For instance, Lazaratos & Marion (1997) presented the time-lapse seismic velocity changes due to CO<sub>2</sub> injection at Chevron's McElroy Field in West Texas, USA. Daley *et al.* (2008), Zhang *et al.* (2012), and

Ajo-Franklin et al. (2013) used crosswell seismic tomography to identify a CO<sub>2</sub> plume. Crosswell seismic surveys are also useful for high-resolution subsurface characterization and exploration of, for example, aquifers (Daley et al., 2004) and nickel sulphide deposits (Greenhalgh et al., 2003). Tube waves are sometimes observed during crosswell surveys, although not as commonly as during single-well surveys because sources and receivers are installed in different wells. When observed, frequency-wavenumber (FK) filters are often used to suppress them before analyzing body waves (Afanasiev et al., 2014). Scattered crosswell tube waves and borehole Mach waves have also been studied (e.g., Cheng et al., 1994; de Hoop et al., 1994; Wu & Harris, 2004). As explained below, borehole Mach waves propagate with the same velocity as tube waves in crosswell surveys.

More than 10,000 tons of CO<sub>2</sub> was injected at 1100 m depth during the Nagaoka surveys (Xue et al., 2006), and time-lapse crosswell seismic travel-time tomograms clearly show the velocity changes associated with the CO<sub>2</sub> injection (Saito et al., 2006; Spetzler et al., 2008; Onishi et al., 2009). Although tube waves during this set of surveys are unusually strong, they have not yet been studied in detail because the surveys were primarily designed for seismic P-wave travel-time tomography. Here, we first introduce the data observed during these crosswell surveys. Then we characterize the tube waves as doubly scattered waves based on their moveouts, amplitudes and synthetic modeling. Next, we leverage the sensitivity of tube waves to the structure and source-receiver distance along the borehole directions to accurately estimate the locations of sources and receivers in the boreholes during each monitoring stage. We also invert waveform envelopes to infer scatterer locations and their scattering coefficients. Finally, we propose and apply a method to estimate subsurface velocities using such tube waves.

## 2 OBSERVED WAVEFIELD DATA

### 2.1 Background of experiment

The crosswell seismic surveys were conducted at Nagaoka, Japan in 2003–2005 to monitor seismic velocity changes associated with CO<sub>2</sub> injection using crosswell seismic travel-time tomography (Figure 1). A total volume of 10,400 tonnes of CO<sub>2</sub> was injected into a porous sandstone layer

of the Haizume formation at 1100 m depth at a rate of 20–40 tonnes per day (Xue et al., 2006). The injection site is located in the Minami-Nagaoka gas and oil field, where several-kilometer thick sedimentary layers exist. Detailed geologic information of the site is discussed by Xue et al. (2006).

Three monitoring wells located around the injection well were instrumented with OYO Wappa multidisc-type downhole mechanical seismic sources (Yokota et al., 2000) and hydrophones as receivers (Figure 1). Well casings were primarily steel; however, fiberglass reinforced plastic (FRP) was used at 950–1204 m measured depth (MD), 1045–1143 m MD, and 928–1156 m MD in wells 2, 3, and 4, respectively. Wells were closely spaced at the surface and diverging with increasing depth (Figure 1). Eight repeated crosswell seismic surveys were conducted. Baseline data were acquired before CO<sub>2</sub> injection began, and seven monitoring surveys were conducted during and after injection (Table 1) (Saito et al., 2006). Three source-receiver geometries were used: (1) Wells 2 and 3, (2) Wells 2 and 4, and (3) Wells 3 and 4, in which the first well mentioned for each configuration refers to the source well and the second refers to the receiver well (Figure 2). Configuration (1) was used for all eight stages, and Configurations (2) and (3) were used for monitoring stages 4, 5 and 7 (Table 1). Data were acquired by a 92-meter 24-sensor hydrophone array with 4 m spacing, and hence four different shots at one location are needed to cover the entire receiver locations. A sequence of shots was carried out at 4 m intervals from the bottom to the top of the well for one hydrophone location before the hydrophone array was redeployed at a new location. Shot records were 1.0 s long for Configuration (1) and 0.5 s long for Configurations (2) and (3). All data were sampled at 0.125 ms interval (Figures 2 and 3).

## 2.2 Identification of wavefields

### 2.2.1 Linear moveout

Direct waves are very weak relative to later arrivals in both source and receiver gathers (Figure 3ab); however, we observe P-waves with hyperbolic moveout (Figure 3ef) in the first 0.12 s, which have been used for travel-time tomography (Saito et al., 2006). Waves with predominant frequency content between 100 and 300 Hz (Figure 4) propagating with nearly linear moveout

**Table 1.** Locations of sources and receivers at each monitoring stage. The numbers are measured depth in meters of the first and last source/receiver. The numbers in parentheses indicate the number of sources or receivers deployed in each well.

Configuration	source well		Stages						
	receiver well	baseline	monitoring 1	monitoring 2	monitoring 3	monitoring 4	monitoring 5	monitoring 6	monitoring 7
1	Well 2	900–1284 (97)	900–1284 (97)	900–1284 (97)	900–1284 (97)	900–1212 (79)	900–1212 (79)	900–1208 (78)	900–1068 (43)
	Well 3	900–1228 (83)	900–1228 (83)	900–1228 (83)	900–1228 (83)	900–1228 (83)	900–1228 (83)	900–1228 (83)	900–1228 (83)
2	Well 2					900–1212 (79)	900–1212 (79)		900–1208 (88)
	Well 4					880–1228 (88)	880–1228 (88)		880–1228 (88)
3	Well 3					900–1212 (79)	900–1088 (48)		900–1212 (89)
	Well 4					880–1228 (88)	880–1228 (88)		880–1228 (88)

(LMO) dominate the gathers after 0.3 s. As explained below, we interpret these as tube waves. These tube waves have interesting features. First, their amplitudes exhibit little temporal decay, and the strongest tube waves are observed around 0.6–0.8 s in the receiver gather (Figure 3a). Note that we do not apply any amplitude correction. Second, the moveout of most tube waves appears independent of the shot and receiver locations, which suggests that they are primarily traveling upward in the source well and downward in the receiver well. The moveouts of tube waves are very similar each other for different well pairs, which implies different wells have similar tube-wave velocities (Figure 2).

Borehole Mach waves, which are similar to aerodynamic Mach waves, can be observed with LMO for crosswell geometries (Meredith et al., 1993; Cheng et al., 1994). Borehole Mach waves are generated when the Stoneley-wave velocity is greater than the shear-wave velocity of the formation, which causes the Stoneley wave to radiate into the formation as a shear wave. In the crosswell surveys, because the receiver well records wavefields of the Mach cone, the moveout is linear and the velocity is the same as the Stoneley wave along the source well. However, we dismiss the possibility that the tube waves in Figure 3 are Mach waves, because the Mach waves decay rapidly and they propagate in the same direction on both source and receiver wells.

When we apply the LMO correction with a velocity of 1.40 km/s, which is a typical velocity for tube waves (Schoenberg et al., 1981), most suspected tube waves become nearly vertical in Figure 3cd. The casing affects the tube-wave velocities, as the velocity of the segments with steel

casing is higher than those of the FRP casing. We estimate more accurate velocities for each casing using beamforming in the next section. The source gathers manifest more complicated waveforms than the receiver gathers because of the acquisition system (Figure 3d). Because of the 92-meter 24-sensor array, we have to concatenate different shots at the same shot location (but at four different times) to create a complete shot gather. Reflected tube waves are generated at the bottom of the receiver array, where a weight keeps the array cable taut.

### 2.2.2 *Velocity of tube waves*

We apply beamforming to the tube waves using slant stacking along the borehole to estimate the tube-wave propagation velocities and compare them to semi-analytically estimated velocities (Rost & Thomas, 2002). This analysis helps confirm that the waves are indeed tube waves. Because the velocities are dependent on the casing materials, we apply beamforming to data separately for well segments with FRP and steel casing. Beamforming analysis reveals that tube-wave velocities differ by about 10% between well segments with FRP and steel casings (Figure 5a). Although the casing is thin, the tube waves are very sensitive to it (Schoenberg et al., 1981). Semi-analytical solutions show that a simple three-layer model, comprising fluid, casing, and host formation (Figure 5b; Wang and Fehler, 2018), can account for the observed tube-wave velocities. Formation velocities are calculated based on the well-log data (Xue et al., 2006), and FRP material parameters are given by Landesmann et al. (2015). Also in agreement with our observations (Figure 4) and supported by previous studies (e.g., Schoenberg, 1986), the very modest frequency dispersion behaviour of the tube-wave velocities is yielded by this semi-analytical calculation. The modeled velocities match the observed data given by the beamforming well. Therefore, we conclude that the downgoing waves with LMO arriving at about 0.3 s and later in Figure 3 are tube waves. We discuss the early LMO waves in the Discussion section.

### 2.2.3 *Doubly scattered tube waves*

Based on the discussion above, the tube waves in Figure 3ab are strong, directional Stoneley waves rather than Mach waves. Thus, tube waves propagating upward in the source well, transfer

to the receiver well, where they propagate downward. Doubly scattered tube waves are the simplest model that accounts for these features (Figure 6). In this model, the waves propagate as tube wave → body wave → tube wave with two conversions between the source and the receiver. Unlike body waves, whose amplitudes decay due to geometrical spreading, tube-wave amplitudes do not exhibit decay caused by such spreading (Herman et al., 2000). Because the wells are closely spaced in the shallow subsurface, the distance over which these waves propagate as body waves is short, and amplitude decay is thus limited. Therefore, we conjecture that the conversion of strong doubly scattered tube waves occurs primarily in shallow well segments. This explains why the late-arriving tube waves are upgoing in the source well and downgoing in the receiver well, and amplitudes stay large. The similarity of travel-time perturbations of tube waves among all combinations of sources and receivers between 0.1–0.7 sec after LMO correction (Figure 7) indicates that the propagation of these waves within the source and receiver arrays is consistent over time. Although even higher-order scattered waves may exist in the data, such waves are much weaker than doubly scattered waves because of scattering coefficients and longer body-wave paths.

### 3 REPOSITIONING OF SOURCES AND RECEIVERS

Location errors for sources and receivers are one of the largest sources of uncertainty in cross-well time-lapse seismic surveys. Accurately estimating these locations is made difficult by the non-uniqueness of the inverse problem, i.e., the trade-off between changes in the source/receiver locations and propagation velocity. Tube waves, however, provide a unique opportunity to improve the location estimates because they are highly sensitive to the location changes made parallel to the borehole.

The wavefields at different monitoring stages are similar to each other but temporally shifted (Figure 8). The magnitude of the temporal shift varies between the direct and tube waves, and the tube waves have larger shifts, which indicates that the shift is caused primarily by the source/receiver location shift rather than changes in the source-onset time.

The relative time shift of tube waves is independent of whether an earlier or later segment of the seismogram is being examined. The relative time shift between two monitoring stages can be

accurately measured by cross-correlating short segments of data. We cross-correlate each 0.02-s segment of the data, and the resultant correlation coefficients for waves from any two stages are predominantly greater than 0.9 (Figure 9c-d). Time shifts appear independent of the casing materials (short dotted lines in Figure 9ab), but dependent on the receiver arrays (short solid lines). This shot gather comprises four shots recorded by different receiver positions. When acquiring data, sources were moved first before receivers. The position of the receiver array was fixed, and a sequence of shots were carried from the bottom to the top of the borehole. Then the receiver array was relocated for another set of sources. Therefore, the error of source locations varies between different receiver-array locations (e.g., receivers above and below the short solid white lines in Figure 9).

We estimate the source and receiver location errors using the time shifts from Figure 9. The errors show the relative deviation of locations between stages, which may be caused by technical limitations, unknown thermal conditions and/or human errors. The time shift,  $\Delta t_{i,J_j}^{k,l}$ , between stages  $k$  and  $l$  can be defined as

$$\Delta t_{i,J_j}^{k,l} = t_{i,J_j}^k - t_{i,J_j}^l = (\Delta s_i^{k,l} + \Delta r_{J_j}^{k,l}) / v + \Delta o_i^{k,l}, \quad (1)$$

where  $J$  is the receiver array,  $i$  is the source,  $j$  is the receiver index within the  $J^{\text{th}}$  array,  $s$  and  $r$  are the source and receiver locations, respectively,  $v$  is the propagation velocity of the tube wave, and  $o_i$  is the onset time for the  $i^{\text{th}}$  source. The symbol  $\Delta$  indicates the difference of a quantity between two stages, and terms without  $\Delta$  represent the shift at each stage; for example,  $\Delta r^{k,l}$  is the receiver location shift between the  $k^{\text{th}}$  and  $l^{\text{th}}$  stages, and  $r^k$  is the receiver location shift at  $k^{\text{th}}$  stage.

Theoretically, the source onset time error  $\Delta o$  can be estimated using the difference in time shifts of the direct wave and tube waves; however, because the signal-to-noise ratio (SNR) of the data is low, time shifts for the direct waves are difficult to estimate reliably. By visually inspecting the direct-wave time shifts in Figure 8, we conclude that the onset time error is negligible ( $\Delta o \sim 0$ ). In this study, we only invert for the location errors.

To estimate the location errors, we assume that the position of receivers along the array remains constant and estimate a single receiver location error per receiver array ( $\Delta r_{J_0}^{k,l} = \Delta r_{J_1}^{k,l} = \dots =$

$\Delta r_{J_j}^{k,l} = \Delta r_J^{k,l}$ ). Moreover, by assuming that the location error is random and the average of the errors is nearly zero, the average of time shifts over all sources and all receivers in each array provides the location error of each receiver array ( $\sum_{i,j}(\Delta t_{i,J_j}^{k,l})/N_i N_j = \sum_{i,j}(\Delta s_i^{k,l} + \Delta r_{J_j}^{k,l})/v N_i N_j = \Delta r_J^{k,l}/v$ , where  $N$  is the total number of sources or receivers in an array). The first assumption is valid because the hydrophone cable is sufficiently elastic. The validity of the second assumption, however, is not guaranteed, although the results shown below support our assumption. After we correct the locations of the receiver arrays, the average of the time shifts over all receivers in each array provides source-location errors ( $\sum_j(\Delta t_{i,J_j}^{k,l} - \Delta r_J^{k,l}/v)/N_j = \sum_j(\Delta s_i^{k,l} + \Delta r_{J_j}^{k,l} - \Delta r_J^{k,l})/v N_j = \Delta s_i^{k,l}/v$ ). Note that source locations may differ per receiver array, even though they were expected to remain at a constant depth.

Because wavefields correlate strongly (correlation coefficients > 0.9), we focus on the first five monitoring stages for Configuration 1 (Table 1). Ten different stage combinations are available for this estimation because we have data for five independent stages. We apply a simple least-squares inversion to relocate sources and receivers at each stage. For example to estimate the receiver array location errors,

$$\Delta \mathbf{t} = \mathbf{G} \mathbf{t}, \quad (2)$$

where

$$\Delta \mathbf{t} = (\Delta t_1^{1,2}, \Delta t_1^{1,3}, \dots, \Delta t_2^{1,2}, \dots, \Delta t_J^{k,l}, \dots)^T, \\ \mathbf{G} = \begin{pmatrix} -1 & 1 & 0 & \dots & 0 & 0 & \dots & 0 & 0 & \dots \\ -1 & 0 & 1 & \dots & 0 & 0 & \dots & 0 & 0 & \dots \\ \vdots & & & & & & & & & \\ 0 & 0 & 0 & \dots & -1 & 1 & \dots & 0 & 0 & \dots \\ \vdots & & & & & & & & & \\ 0 & 0 & 0 & \dots & 0 & 0 & \dots & -1 & 1 & \dots \\ \vdots & & & & & & & & & \end{pmatrix}, \\ \mathbf{t} = (t_1^1, t_1^2, \dots, t_2^1, \dots, t_J^k, \dots)^T,$$

and we calculate  $\Delta t_J^{k,l} = \sum_{i,j} \Delta t_{i,J_j}^{k,l} / N_i N_j$  and  $t_J^k = \sum_{i,j} t_{i,J_j}^k / N_i N_j = r_J^k / v$ . We can compute the time shift at each stage with  $\mathbf{t} = (\mathbf{G}^T \mathbf{G})^{-1} \mathbf{G}^T \Delta \mathbf{t}$  using a pseudoinverse matrix for  $(\mathbf{G}^T \mathbf{G})^{-1}$ . Note that because we estimate relative errors, we do not define the origin point of  $r$ . We use a similar expression for source locations.

After solving the inverse problem, time shifts are converted to location errors using the velocities  $v$  estimated by beamforming (Figure 5). The array location changes between monitoring stages, and at each monitoring stage, the variation in the location errors among four different receiver arrays is small (Figure 10). The mean values for source locations are close to zero, and their error distribution is nearly normal, which supports our second assumption about average time shifts (Figure 10b). Overall, the location errors are small (less than tens of centimeters) for both sources and receivers, but measurable using tube waves. Hence, the resulting errors in the distance between sources and receivers are largely negligible for body-wave applications. The average standard deviation of the offset errors for all stages, which is important for travel-time tomography, is only 0.13%. We repeat this inversion for all available stages during experiment Configurations 2 and 3, and correct the location errors. We use the corrected locations for the analyses below, unless otherwise noted.

#### 4 LOCATION OF TUBE-WAVE SCATTERERS

Our interpretation of late-arriving tube waves being doubly scattered waves requires the existence of at least one scatterer for each well (Figure 6). The long train of tube waves indicates that, in fact, many scatterers exist along the wells. These scatterers may be fractures, lithological layers, or variations in well characteristics (Minato *et al.*, 2017). In this section, we estimate the location of scatterers using late-arriving tube waves for all experimental configurations (Table 1). To estimate scatterer locations with a reasonable computational cost, we first average LMO corrected wavefields over all sources and receivers at each well pair for increasing SNR of waves (i.e., averaging wavefields along the source and receiver axes in Figure 7, but with more accurate velocities estimated in Figure 5). This averaging assumes that the tube waves are propagating inside of arrays with the estimated velocity, and that no scatterers exist within the array. After this averaging, we

obtain three waveforms and compute their envelopes, one per survey configuration (Figure 11). Because of the convention of our LMO correction, the waves in Figure 11 can be considered as the wavefield between the shallowest receiver and source at each well pair. These envelopes are treated as observations in our inversion for estimating the scatterer locations described below.

For given scatterer locations in each well, we can calculate synthetic envelopes of the doubly scattered waves using the model in Figure 6. We invert for the true scatterer locations by comparing the envelopes of synthetic waveforms against the observed data described in the paragraph above. Our inversion minimizes the average over all well pairs of the  $\ell_2$  norm of the difference between synthetic and observed waveform envelopes. We use the envelopes instead of the true wavefields to mitigate the problem of phase changes due to scattering of the unknown source functions. For this wavefield synthesis, we use a Ricker wavelet source with the central frequency of 150 Hz based on observation (Figure 4), and we convolve three Green's functions—a) a tube wave from the source to the first scatterer, b) a body wave between two scatterers, and c) another tube wave from the second scatterer to the receiver—to obtain the target waveform. Here we use the two tube-wave velocities estimated by casing-dependent beamforming analysis (Figure 5a) and P-wave velocity of 2.3 km/s based on well-log data (Onishi et al., 2009). We do not consider attenuation of waves, but do include the geometrical spreading effect for body waves.

First, we use a grid search to determine the depth and scattering coefficient of a single scatter in each well. The grid search ranges between 400 and 1250 m depth with 1 m interval and -1 to +1 with 0.05 interval for the scattering coefficient. We analytically calculate doubly scattered tube waves and compare their envelope to observed data to find the best set of scattering parameters (depth and scattering coefficient) for each well. Then, using simulated annealing, we iteratively increase the number of scatterers in each well by one and repeat the grid search to determine whether the objective function decreases as a result of increasing the number of scatterers. Whenever the objective function decreases, we adopt the scatterer; otherwise we discard it. At each iteration, we also refine the location and scattering coefficient of previously located scatterers. After 25 iterations, the inversion converges and we obtain the scatterer properties (Figure 12). The synthetic envelopes agree very well with the observed data for all three well combinations (Figure 11).

The scatterers are concentrated in the shallower well segments, where the well spacing is small. The curvature of wells can be a scattering point (e.g., in wells 2 and 3), but the strongest scattering locations may be caused by other factors, such as fractures or cementing, considering that their locations appear independent of the well shape. Information on well integrities, borehole caliper, and fracture locations is unfortunately unavailable. The observed tube waves are insensitive to very shallow scatterers because of the record lengths. Note that if we only have two wells, this inverse problem is strongly non-unique. The third well, however, provides additional constraints into the inversion because the same scatterers must match two independent envelopes. A few scatterers are located within the source and receiver arrays (Figure 12), which deviates from our assumption of no scatterers existing within the arrays, but because the coefficients are small, we consider this to be a numerical error with negligible effect on the synthetic envelopes.

## 5 SUBSURFACE VELOCITY ESTIMATION

We use these doubly scattered tube waves to estimate subsurface velocities. Because the tube waves encode information about subsurface properties around the well in addition to casing materials (Tezuka *et al.*, 1997), we can use them to extract subsurface velocities around the borehole. With the analyses above, most of the tube waves in Figure 7 repeatedly propagate along the source and receiver arrays. This repeated propagation provides rich information from which wave velocities along the arrays can be computed.

When we deconvolve tube waves generated by two sources in Well 2 and observed by one receiver in Well 3, we can extract wave propagation effects between these sources (Nakata & Snieder, 2012). Because deconvolution numerically removes the path effects between the receiver and the closest source used, we average the deconvolved wavefields over all receivers to extract reliable wavefields between the sources. We repeat this deconvolution between all source pairs and then estimate the interval velocities along the source well from the travel times of deconvolved waveforms (Figure 13a). The estimated velocities agree very well with the trend shown in the well-log data, particularly the gradual increase in velocities with increasing depth and the high velocity zones at 1000 m, 1040 m, and 1155 m depths. In this area, S-wave velocities are

about half of the P-wave velocities, and tube wave velocities are almost the same as for S-waves based on our numerical calculation using the algorithm from Wang & Fehler (2018) (Figure 13b). Using this numerical solver, we can potentially invert for the S-wave velocities from tube-wave velocities; however this is beyond the scope of this work. Regardless, Figure 13a shows that tube waves provide useful signals for estimating velocities around the wellbore, even when well-log data are unavailable. We can also estimate velocities along the receiver well using reciprocity and computing deconvolutions between receivers instead of sources.

Interestingly, tube waves can resolve neither the very high-V<sub>p</sub> silt layer at 1100 m depth nor the velocity decrease in the reservoir due to the CO<sub>2</sub> injection immediately below the silt layer (also see the black lines in Figure 14). This is possibly because the high-V<sub>p</sub> layer and the reservoir are too thin (around 3 m and 6 m, respectively, based on Xue et al. (2006)) compared to the wavelength of the tube waves ( $\sim 10$  m) and receiver spacing (4 m). Neither can the synthetic tube waves obtained by the numerical solution of Wang & Fehler (2018) (blue in Figure 13a) resolve the high V<sub>p</sub> layer either.

In Figure 13a, we downsample the well-log data to directly compare the results with field observations. The resolution limit is partly due to the receiver spacing, and we test the sensitivity of tube waves to thin layers when we have very dense borehole receivers, such as would be provided by distributed acoustic sensing. When we assume that the receiver spacing is the same as the well-log sampling (15 cm), the tube waves can capture the silt layer at 1100 m, although the absolute values are much smaller (Figure 13b).

Because our method uses time shifts between different monitoring stages for correcting source and receiver locations, we cannot use the location corrected data for time-lapse monitoring of the structure. Note that we can, however, still use the corrected locations for body-wave seismic tomography. Because the estimated location errors are relatively small (Figure 9), we compute tube-wave velocities at each monitoring stages without repositioning (Figure 14). At each stage, the velocities estimated from tube waves agree well with the well-log velocities. General trends and layers at 1000 m and 1040 m are well resolved, but, similar to Figure 13a, the silt and velocity reduction at 1115 m due to the CO<sub>2</sub> injection cannot be imaged. The tube waves may be insensitive

to the reservoir because it is too thin, as discussed above. It may also be the case, however, that tube waves are insensitive to the CO<sub>2</sub> injected in this experiment because tube waves are most sensitive to S-wave velocities and injected CO<sub>2</sub> does not modulate the subsurface shear modulus, unless injection results in pore-pressure or large density changes.

## 6 DISCUSSION

### 6.1 Early linear-moveout waves

At earlier times, close to the direct P-waves, similar LMO waves exist, particularly in the receiver gather (white arrows in Figure 3ef). These waves may be considered as converted tube waves excited by direct body-wave arrivals (Schoenberg, 1986) for which the conversion is caused by local fractures around the receiver well or the effect of wellbore roughness (Bouchon & Schmitt, 1989). Although this body-tube converted wave may exist, as presented by Wu & Harris (2004), we suspect that most of these waves here are likely SP converted waves, which are excited as S waves at a source, scattered and converted to P waves, and then observed at a receiver.

We model the SP wavefields numerically and their travel times semi-analytically in Appendix A. Interestingly, the SP waves look very different in the source and receiver gathers and have almost linear moveout in the receiver gather (Figure A2). The OYO Wappa source usually excites P waves predominantly (Yokota *et al.*, 2000), but source-borehole coupling is complicated by the directional wells, and P and S waves may possibly both be generated by the source as a result (Nakata *et al.*, 2022). PS converted waves might exist but are invisible, because hydrophones are insensitive to S waves. This would also explain why more LMO waves are observed in the receiver gather (Figure 3e) than in the source gather (Figure 3f). This phenomenon additionally indicates the importance of simultaneously interpreting both shot and receiver gathers for identifying wavefields.

### 6.2 Inversion of scatterers

The inversion for estimating scatterer locations and reflection coefficients employs a grid search, which can be computationally expensive as they are a brute-force approach. The computational

cost of our inversion, however, remains modest because we use simulated annealing to find values for each scatterer and averaged envelopes as input data. This averaging reduces the size of the input data and computational cost of forward modeling. We also mitigate the effect of local minima by using envelopes instead of actual wavefields. In this study, this inversion takes several hours to run on a laptop.

Our lack of knowledge of the source wavelet is another limitation in our inversion. We use a Ricker wavelet because it is a relatively simple wavelet which represents the Wappa source well. The radiation pattern of tube waves for particular borehole sources is often not studied; however, our inversion would benefit significantly if such information were available.

We discuss the scattering effect of tube waves due to fractures and geological structures. Fractures can also trap seismic energy and generate guided waves (e.g., Liang et al., 2017). The amplitudes of the guided waves are potentially large because of a small geometrical spreading effect. Therefore, if a large fracture exists across multiple wells, such guided waves may be observed. We do not include such waves in our modeling because we do not have evidence of the existence of such large fractures in this study.

### **6.3 Joint inversion of velocities and source/receiver locations**

We implement a two-step procedure to estimate the source and receiver positions and subsurface velocities. This workflow prevents us from estimating time-lapse velocities after repositioning sources and receivers. Position errors and subsurface velocities could potentially both be solved simultaneously; however, doing so would increase the non-uniqueness in the inverse problem. For example, we could consider the velocity as a known parameter in equation 1. Alternatively, the velocity can be treated as an unknown function of locations along the boreholes. We do not try this large inversion though because the quality of our data is limited. Note that we estimate the location errors between stages and subsurface velocities within each stage. After we estimate the time shift with cross-correlation, we can jointly invert for velocity and locations.

## 7 CONCLUSIONS

We find anomalously strong downgoing tube waves in a crosswell seismic monitoring survey, and infer that they are related to second-order scattered tube waves. The observed tube waves differ from borehole Mach waves and body-to-tube converted waves based in that they are long lived and exhibit little amplitude decay. All strong tube waves observed propagate in one direction. We apply beamforming to the tube waves to accurately estimate velocities, and casing materials affect the velocities significantly. Semi-analytical synthetic tube wave modeling is well-matched to observations, and confirms their nature. Based on the well trajectories, we infer that most scatterers are located in the shallow segments of the wells (above the sources and receivers) and the tube waves have uniform LMO, in which the waves are always upgoing in the source well and downgoing in the receiver well.

Using these scattered tube waves, we estimate accurate source and receiver locations for different monitoring stages. We overcome one of the most common problems for time-lapse surveys: the location error. For this survey, the position errors are relatively small over different monitoring stages and negligible for body-wave applications such as crosswell travel-time tomography. We invert tube-wave envelopes to determine scatterer locations captured by the doubly scattered waves. We then propose a technique to monitor subsurface velocities with wavefield deconvolution. The estimated velocities agree well with the velocities measured by logging tools.

Based on our knowledge, no studies have presented such enigmatic tube waves at crosswell surveys. These waves are due to the shape of boreholes, source types and the existence of scatterers along the boreholes. We demonstrate here that the tube waves can provide accurate source and receiver locations, which are not easy to estimate from other wavefields, as well as subsurface information such as scatterers and geology. These tube waves can potentially be used to increase the accuracy of time-lapse tomography for monitoring CO<sub>2</sub> subsurface sequestration.

## 8 ACKNOWLEDGEMENTS

We thank RITE for providing the dataset. Nafi Toksöz, Arthur Chang, and Zhao Zheng provided valuable comments about tube waves. We are grateful to Hua Wang to provide us the code to

compute synthetic tube waves. Editor Cornelis Weemstra and two anonymous reviewers provided fruitful comments to improve the quality of the manuscript. This study is partly supported by JOGMEC.

## **9 DATA AVAILABILITY STATEMENT**

The data underlying this article will be shared on a request with collaboration to the 4th author (Ziqiu Xue).

## References

- Afanasiev, M. V., Pratt, R. G., Kamei, R., & McDowell, G., 2014. Waveform-based simulated annealing of crosshole transmission data: A semi-global method for estimating seismic anisotropy, *Geophys. J. Int.*, **199**(3), 1586–1607.
- Ajo-Franklin, J. B., Peterson, J., Doetsch, J., & Daley, T. M., 2013. High-resolution characterization of a CO<sub>2</sub> plume using crosswell seismic tomography: Cranfield, MS, USA, *Int. J. Greenh. Gas Control*, **18**, 497–509.
- Bakku, S. K., Fehler, M., & Burns, D., 2013. Fracture compliance estimation using borehole tube waves, *Geophysics*, **78**(4), D249—D260.
- Bickle, M. J., 2009. Geological carbon storage, *Nat. Geosci.*, **2**(12), 815–818.
- Biot, M. A., 1952. Propagation of elastic waves in a cylindrical bore containing a fluid, *J. Appl. Phys.*, **23**, 997–1005.
- Bouchon, M. & Schmitt, D. P., 1989. Full-wave acoustic logging in an irregular borehole, *Geophysics*, **54**(6), 758–765.
- Cheng, C. H. & Toksöz, M. N., 1981. Elastic wave propagation in a fluid-filled borehole and synthetic acoustic logs, *Geophysics*, **46**(7), 1042–1053.
- Cheng, N., Zhu, Z., Cheng, C. H., & Toksöz, M. N., 1994. Experimental and finite difference modelling of borehole Mach waves, *Geophys. Prospect.*, **42**(4), 303–319.
- Daley, T. M., Majer, E. L., & Peterson, J. E., 2004. Crosswell seismic imaging in a contaminated basalt aquifer, *Geophysics*, **69**(1), 16–24.
- Daley, T. M., Myer, L. R., Peterson, J. E., Majer, E. L., & Hoversten, G. M., 2008. Time-lapse crosswell seismic and VSP monitoring of injected CO<sub>2</sub> in a brine aquifer, *Environ. Geol.*, **54**(8), 1657–1665.
- de Hoop, A. T., de Hon, B. P., & Kurkjian, A. L., 1994. Calculation of transient tube-wave signals in cross-borehole acoustics, *J. Acoust. Soc. Am.*, **95**(4), 1773–1789.
- Greenhalgh, S., Zhou, B., & Cao, S., 2003. A crosswell seismic experiment for nickel sulphide exploration, *J. Appl. Geophys.*, **53**(2-3), 77–89.
- Herman, G. C., Milligan, P. A., Dong, Q., & Rector, J. W., 2000. Analysis and removal of

- multiply scattered tube waves, *Geophysics*, **65**(3), 745–754.
- Landesmann, A., Seruti, C. A., & Batista, E. D. M., 2015. Mechanical properties of glass fiber reinforced polymers members for structural applications, *Mater. Res.*, **18**(6), 1372–1383.
- Lazaratos, S. K. & Marion, B. P., 1997. Crosswell seismic imaging of reservoir changes caused by CO<sub>2</sub> injection, *Lead. Edge*, pp. 1300—1306.
- Li, Y.-G., Aki, K., Adams, D., Hasemi, A., & Lee, W. H. K., 1994. Seismic guided waves trapped in the fault zone of the Landers, California, earthquake of 1992, *J. Geophys. Res.*, **99**, 11705–11722.
- Liang, C., O'Reilly, O., Dunham, E. M., & Moos, D., 2017. Hydraulic fracture diagnostics from Krauklis-wave resonance and tube-wave reflections, *Geophysics*, **82**(3), D171–D186.
- Meredith, J. A., Toksöz, M. N., & Cheng, C. H., 1993. Secondary shear waves from source boreholes, *Geophys. Prospect.*, **41**, 287–312.
- Minato, S., Ghose, R., Tsuji, T., Ikeda, M., & Onishi, K., 2017. Hydraulic properties of closely spaced dipping open fractures intersecting a fluid-filled borehole derived from tube waves generation and scattering, *J. Geophys. Res.*, **122**, 8003–8020.
- Nakata, N. & Snieder, R., 2012. Estimating near-surface shear-wave velocities in Japan by applying seismic interferometry to KiK-net data, *J. Geophys. Res.*, **117**, B01308.
- Nakata, R., Nakata, N., Girard, A., Ichikawa, M., Kato, A., Lumley, D., & Xue, Z., 2022. Time-lapse crosswell seismic monitoring of CO<sub>2</sub> injection at the Nagaoka CCS site using elastic full waveform inversion, *SEG Exp. Abs.*.
- Onishi, K., Ueyama, T., Matsuoka, T., Nobuoka, D., Saito, H., Azuma, H., & Xue, Z., 2009. Application of crosswell seismic tomography using difference analysis with data normalization to monitor CO<sub>2</sub> flooding in an aquifer, *Int. J. Greenh. Gas Control*, **3**, 311–321.
- Rost, S. & Thomas, C., 2002. Array seismology: Methods and applications, *Rev. Geophys.*, **40**, 1008.
- Saito, H., Nobuoka, D., Azuma, H., Xue, Z., & Tanase, D., 2006. Time-lapse crosswell seismic tomography for monitoring injected CO<sub>2</sub> in an onshore aquifer, Nagaoka, Japan, *Explor. Geophys.*, **37**, 30–36.

- Schoenberg, M., 1986. Fluid and solid motion in the neighborhood of a fluid-filled borehole due to the passage of a low-frequency elastic plane wave, *Geophysics*, **51**(6), 1191–1205.
- Schoenberg, M., Marzetta, T., Aron, J., & Porter, R. P., 1981. Space–time dependence of acoustic waves in a borehole, *J. Acoust. Soc. Am.*, **70**(5), 1496–1507.
- Spetzler, J., Xue, Z., Saito, H., & Nishizawa, O., 2008. Case story: Time-lapse seismic crosswell monitoring of CO<sub>2</sub> injected in an onshore sandstone aquifer, *Geophys. J. Int.*, **172**(1), 214–225.
- Stockwell, R. G., Mansinha, L., & Lowe, R. P., 1996. Localization of the complex spectrum: The S transform, *IEEE Trans Signal Process*, **44**(4), 998–1001.
- Tezuka, K., Cheng, C. H., & Tang, X. M., 1997. Modeling of low-frequency Stoneley-wave propagation in an irregular borehole, *Geophysics*, **62**(4), 1047–1058.
- Wang, H. & Fehler, M., 2018. The wavefield of acoustic logging in a cased-hole with a single casing - Part I: A monopole tool, *Geophys. J. Int.*, **212**(1), 612–626.
- Wu, C. & Harris, J. M., 2004. Cross-well seismic modeling with inclusion of tube waves and tube-wave-related arrivals, *Geophys. Res. Lett.*, **31**(11), 1–4.
- Xue, Z., Tanase, D., & Watanabe, J., 2006. Estimation of CO<sub>2</sub> saturation from time-lapse CO<sub>2</sub> well logging in an onshore aquifer, Nagaoka, Japan, *Explor. Geophys.*, **37**, 19–29.
- Yokota, T., Ishii, Y., Mizohata, S., Shoji, Y., Ohhashi, T., & Ogura, K., 2000. Development of a multi-disk type borehole seismic source—aiming at practical applications for oil field survey, *Geophys. Explor.*, **53**, 309–323.
- Zhang, F., Juhlin, C., Cosma, C., Tryggvason, A., & Pratt, R. G., 2012. Cross-well seismic wave-form tomography for monitoring CO<sub>2</sub> injection: A case study from the Ketzin Site, Germany, *Geophys. J. Int.*, **189**(1), 629–646.
- Zheng, Z., Bland, H., & Machovoe, S., 2018. Frac-hits mapped by tube waves – a diagnostic tool to complement microseismic monitoring, *SEG Expand. Abstr.*, pp. 2887–2891.

## APPENDIX A: SP CONVERTED WAVE

In this section, we model the early linear-moveout waves near the direct waves (Figure 3ef) and show that they are likely SP converted waves. We compare the field data to two types of synthetic

data: elastic modeling with a) isotropic and b) double-couple sources (Figure A1). In both cases, the receivers are hydrophones and the geometry is the same as the one used in the field data. The synthetic data are computed with a 2D finite difference wave-equation solver. The velocity model for this simulation (Figure A1a) is obtained by a spline interpolation of three well-log data (Xue et al., 2006). We use isotropic and double-couple sources, which excite only P wave and both P and S waves, respectively. The nodal plane of the double-couple source is in the horizontal direction without loss of generality.

The first arrivals are modeled for both isotropic and double-couple cases (Figure A1). Because of the low velocity zone, the waves at receivers around 1100 m depth arrive later than those at neighbouring receivers. The hyperbolic wave around 0.15 s in the source gather in Figure A1g resembles the wave in Figure A1c, but the isotropic case does not have such waves in Figure A1e. These waves are SP converted waves, which are excited as S waves by the source, converted to P waves at the sharp velocity contrast at the reservoir, and recorded as P waves at receivers. Interestingly, but probably not very intuitively, these SP waves are recorded as waves with nearly linear moveouts in the receiver gather (Figure A1f). This is the wave also observed in Figure 3ef.

To validate these moveouts (a hyperbolic moveout in the source gather and a linear moveout in the receiver gather) we calculate analytical travel-times of direct P, PP and SP waves with a simple geometry, where source and receiver wells are vertical and a reflector is horizontal (Figure A2). The travel time of the direct P wave,  $t_d$ , is given by

$$t_d = \sqrt{h^2 + (z_s - z)^2} / v_p, \quad (\text{A.1})$$

where  $v_p$  is the P-wave velocity. Other symbols are shown in Figure A2. Similarly, the travel time of the PP wave is

$$t_{PP} = \sqrt{h^2 + (|z_{ref} - z| + |z_{ref} - z_s|)^2} / v_p. \quad (\text{A.2})$$

The PP wave becomes identical to the direct P waves when the source and receiver are on the other side of the reflector ( $z > z_{ref} > z_s$  or  $z_s > z_{ref} > z$ ). For the SP converted wave, the travel time can

be computed using the location of the conversion point  $h_s$  as

$$t_{SP} = \sqrt{|z_{ref} - z_s|^2 + h_s^2}/v_s + \sqrt{(h - h_s)^2 + |z_{ref} - z|^2}/v_p, \quad (\text{A.3})$$

where  $v_s$  is the S-wave velocity. When we calculate the derivative of the SP travel time for the conversion point, we obtain Snell's law.

We calculate the travel times for direct P, reflected PP, and converted SP waves using equations A.1–A.3 with a P-wave velocity of 2500 m/s, an S-wave velocity of 1250 m/s, and a well distance of 150 m (Figure A2bc). In this calculation, we conduct a grid search for the conversion point to minimize the travel time. Similar to the field data, the SP-wave travel time is recorded as a hyperbola in the source gather and is nearly linear in the receiver gather. The moveouts of the direct P and PP waves are, however, identical for both gathers. The difference of moveouts at source and receiver gathers are due to the locations of the conversion points in the gathers. In the source gather, the conversion point does not move much for different receiver locations, so the moveout of the SP waves becomes similar to the time of direct P waves. On the other hand, in the receiver gather, the converted points change across the source locations, and therefore the moveout of the SP waves is more controlled by the S-wave velocity and the travel path of the S-wave segment of the path. We need to pay careful attention to these converted waves because we may misinterpret them as tube waves due to their moveout. The tube wave velocities are also close to the S waves. If we want to use the SP waves, we should use source gathers, or a special pre-processing filter is needed to mute tube waves but retain these converted waves. We find that the receiver gather contains such linear-moyeout waves much more than the source gather. Note that the source can generate S waves, but the receivers (hydrophones) are not sensitive to S waves.

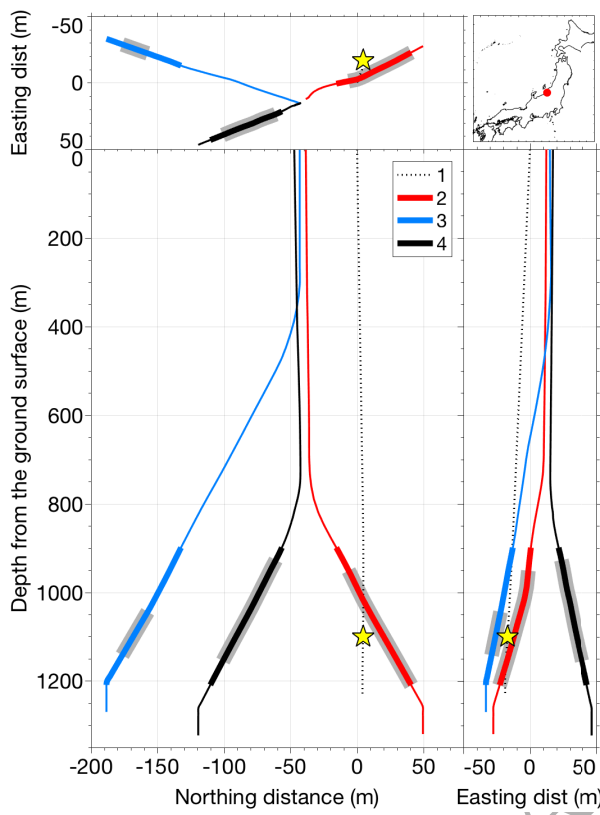


**Figure 1.** Geometry of injection (dashed line, 1) and monitoring wells (solid lines, 2–4). Cross and map sections are shown at each panel. The top-right inset shows the location of our site. The yellow star indicates the location of  $\text{CO}_2$  injection. The thick line at each monitoring well shows the locations of receiver or source array (Table 1). The grey shade shows the zones where FRP is used for casing. Steel casing is used at other zones.

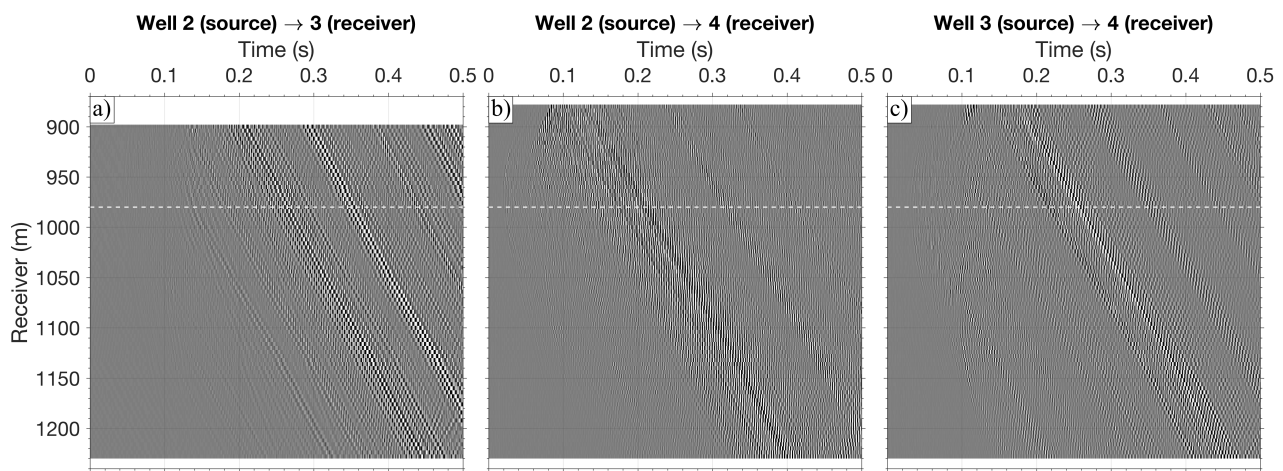


**Figure 2.** Examples of shot gathers at different experiment configurations (Table 1). The white dashed line shows the location of source. The receiver depth is the measured depth along the well.

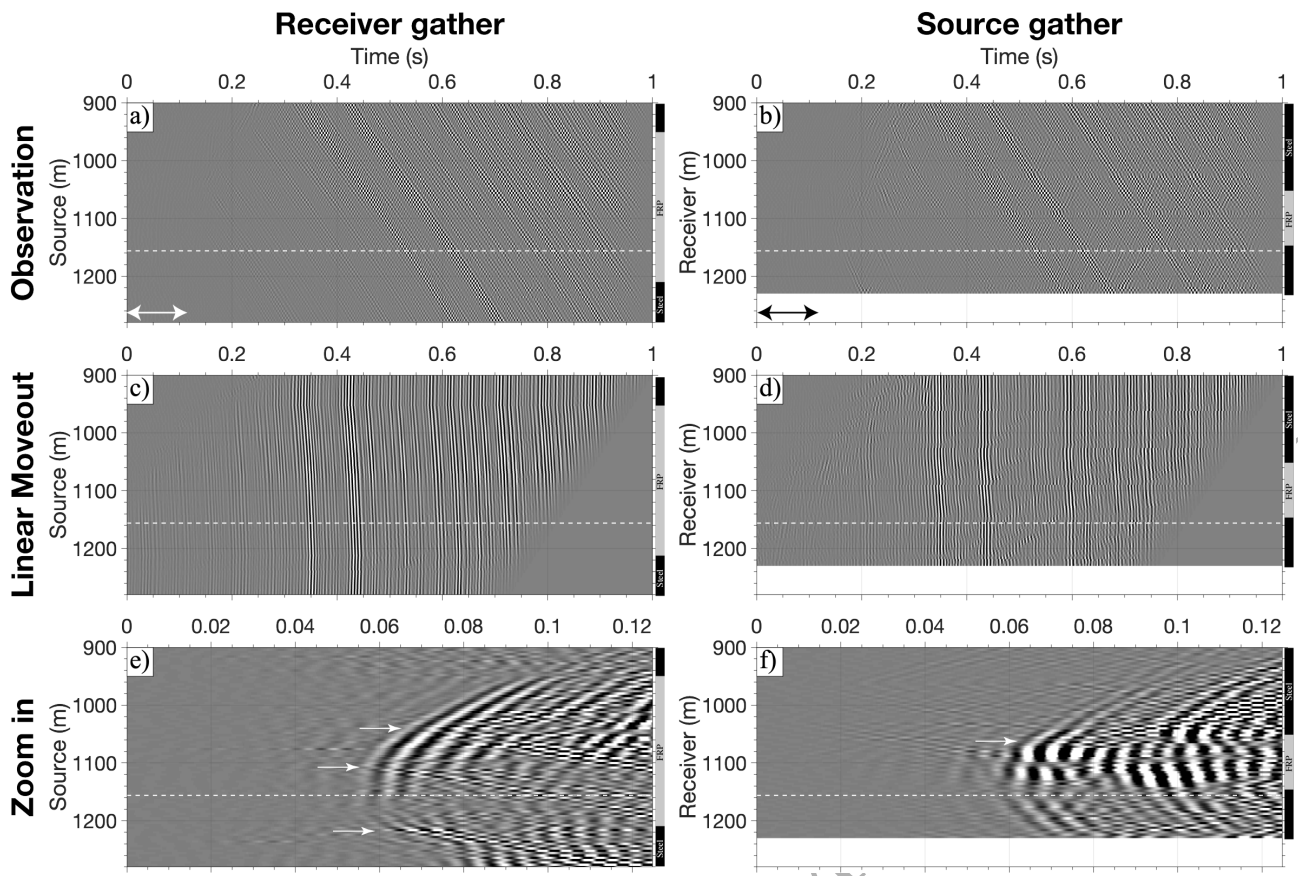


**Figure 3.** Examples of receiver and shot gathers (a,b). Source and receiver wells are Wells 2 and 3, respectively. (c,d) Same waveforms as panels a and b, but after LMO correction with the velocity of 1.40 km/s. (e,f) Zoomed waveforms at the time window highlighted by the arrows in panels a and b. The white rightward arrows show the converted waves discussed in the main text. The white dashed lines show the locations of receiver and source for left and right panels, respectively. The source and receiver depths are the measured depth along the well. The right bars at each panel illustrate the casing materials, and black and gray are steel and FRP casings, respectively. Note that we do not apply any amplitude correction along the time or space axes.

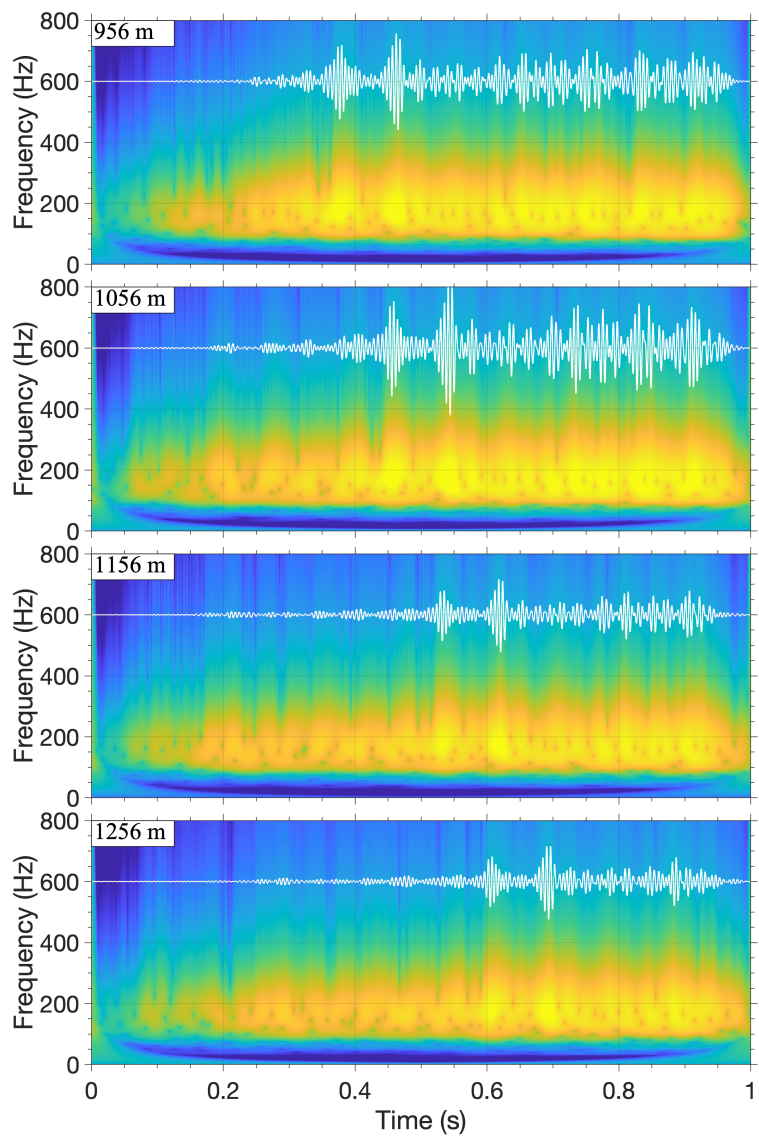


**Figure 4.** Examples of spectrograms of four traces in the receiver gather shown in Figure 3. The spectrograms are computed by S transform (Stockwell et al., 1996). The source location is shown at the top-left corner of each panel. In each panel, brighter color indicates the more powerful signals. The white lines show the time-domain waveforms.

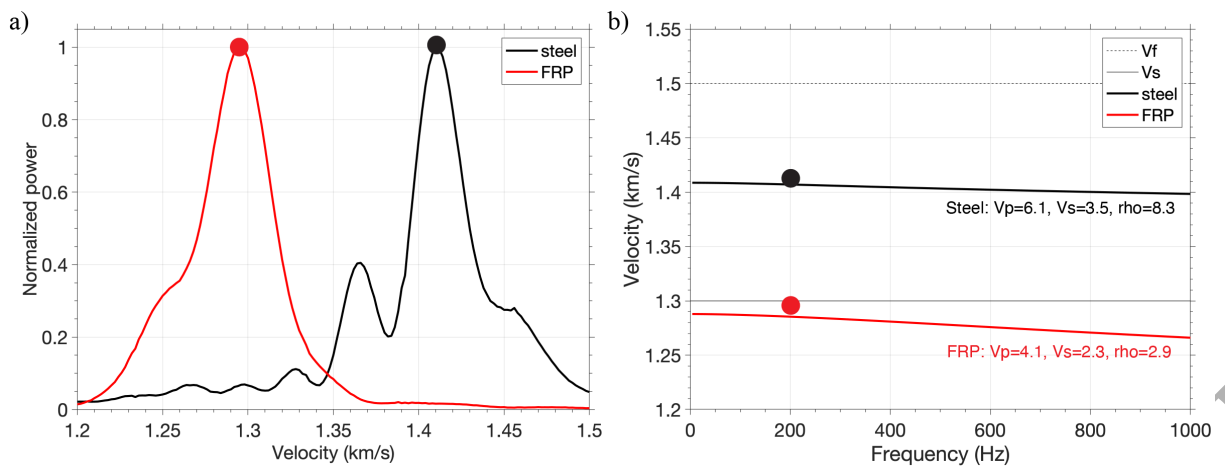


**Figure 5.** (a) Beamformed wavefield power against tube-wave velocities at steel and FRP casing zones. The power is normalized by the maximum power for each casing. The dots show the velocities at the maximum power. The estimated velocities are 1.29 and 1.41 km/s for FRP and steel casing, respectively. (b) Modeled dispersion curves of tube waves for steel (black) and FRP (red) casings. The dotted and thin horizontal lines represent the velocity of the fluid and formation S waves, respectively. The dots show the velocities estimated in panel (a) at the frequency estimated in Figure 4.

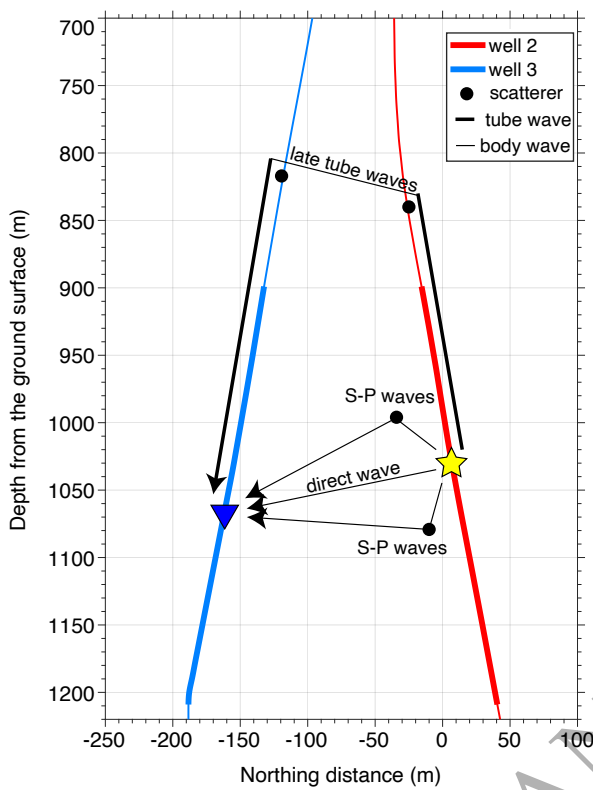


**Figure 6.** Schematic diagram of observed wave paths from a source (yellow star) to a receiver (blue triangle). The black dots indicate scatterers and the arrows wave paths. Thin and thick arrows are body and tube waves, respectively. Note that we use the correct aspect ratio between northing distance and depth.

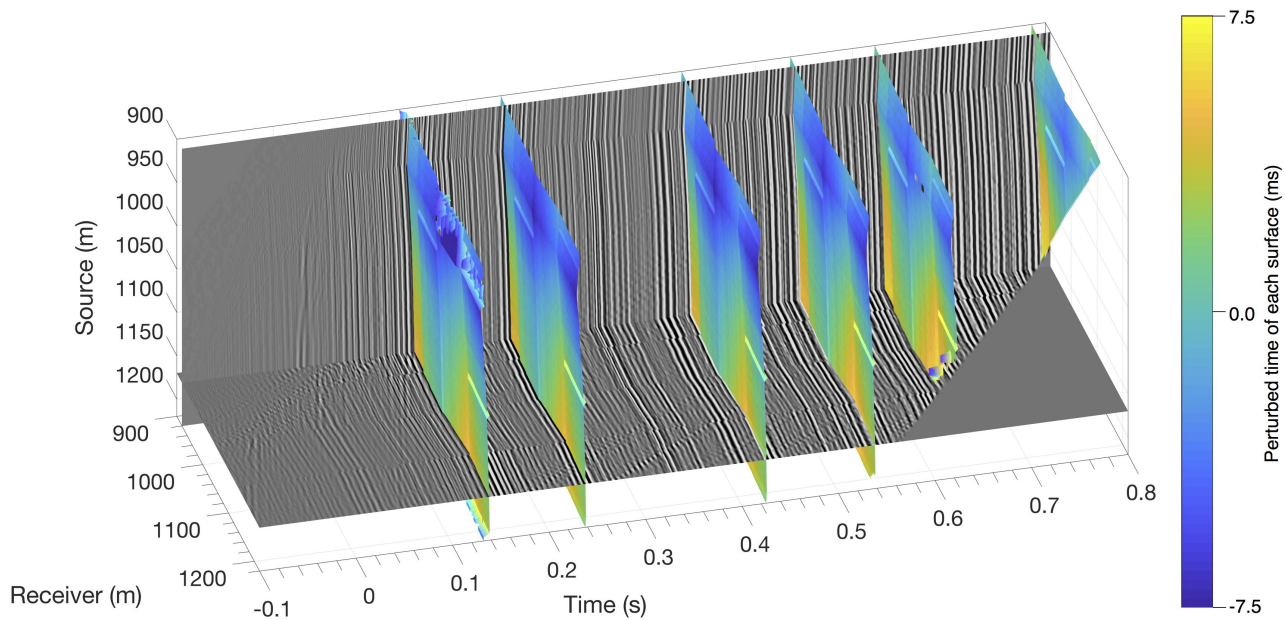


**Figure 7.** Tube wavefields for all sources and receivers after linear moveout correction with the velocity of 1.40 km/s, and two gray slices show constant source or receiver waveforms. We select six prominent tube waves and estimate averaged travel times over entire source and receiver arrays. The colored slices show the deviations of travel times (i.e., perturbed time) from the averaged travel times at each wave.

ORIGINAL UNEDITED

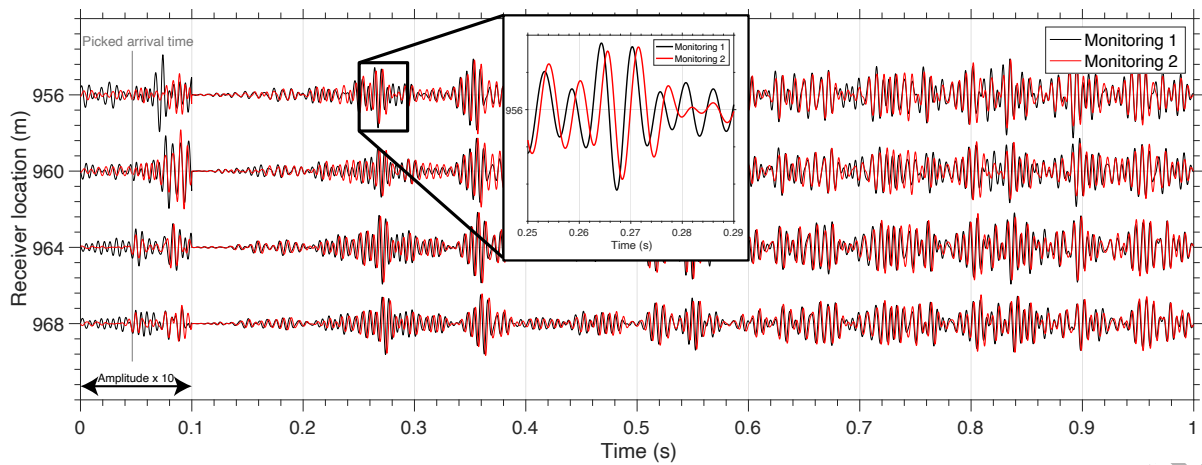


**Figure 8.** Comparison of wavefields between two monitoring stages (black: Monitoring 1, red: Monitoring 2). The inset shows the magnified waves. The amplitudes of waves at the first 0.1-s window are amplified 10 times for visualization purposes. Body waves mainly exist in this time window, and the other waves are mostly tube waves (see Figure 3)ab.

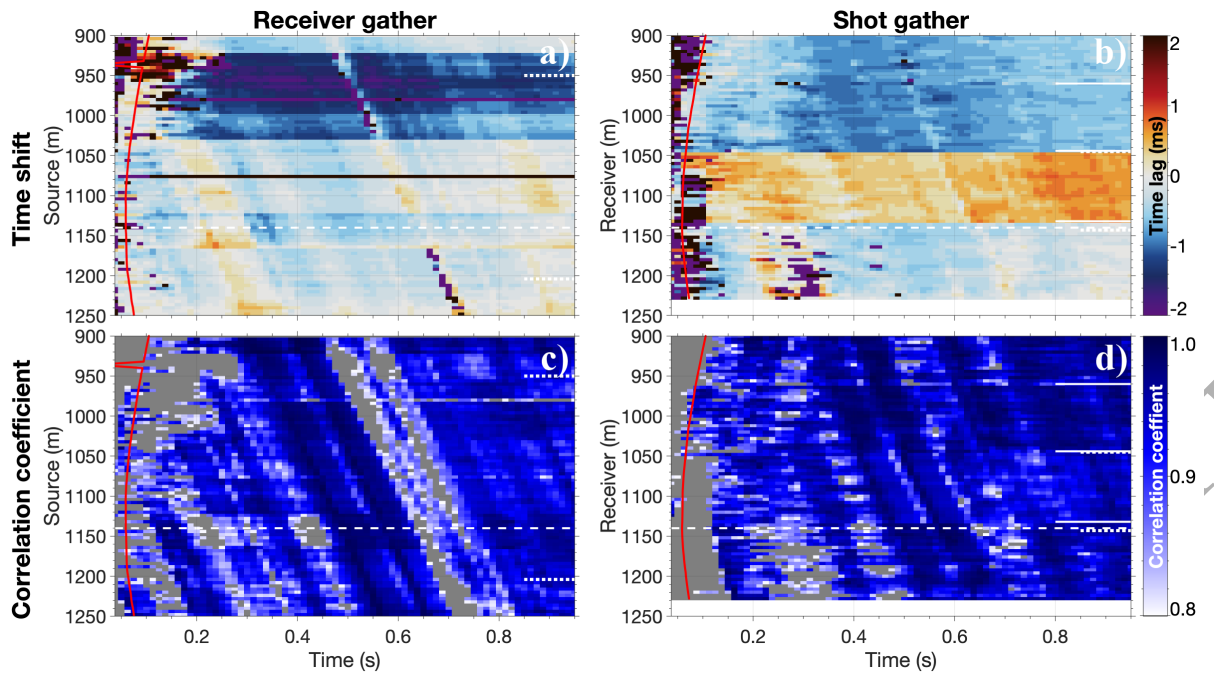


**Figure 9.** Measured time shift (a,b) and correlation coefficient (c,d) between Monitoring stages 1 and 2. Panels (a,c) and (b,d) show receiver and shot gathers. The white dashed lines show the location of source or receiver for each gather. The red line shows the picked arrival time of direct P waves used for travel-time tomography (Saito et al., 2006). The short dotted lines illustrate the location of different casing materials. The short solid white lines on the shot gathers indicate the changes in the receiver arrays, which cause time shifts.

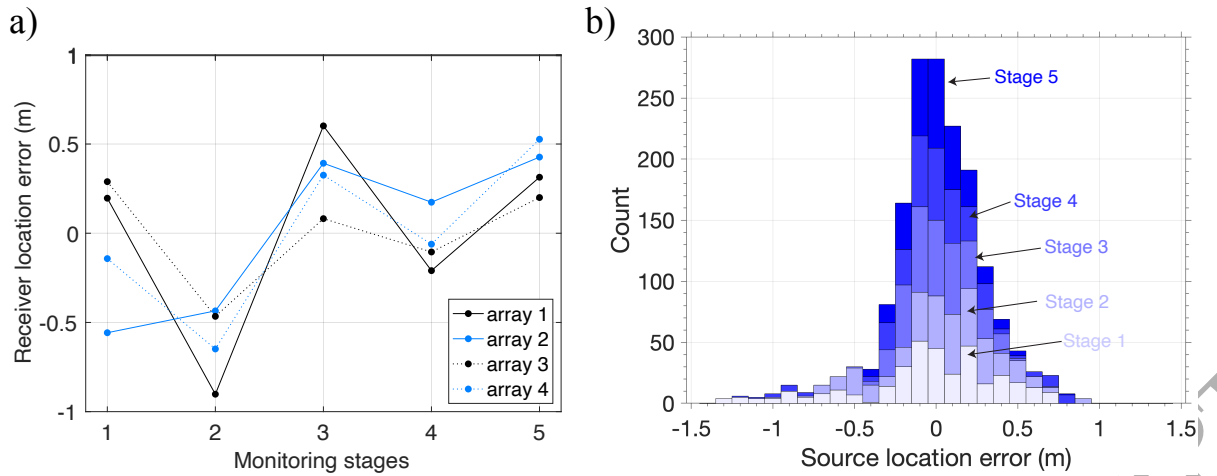


**Figure 10.** Location errors for (a) receiver arrays and (b) sources. The positive error means that the source/receiver is shifted downward. In panel (b), source location errors are estimated for each receiver array but plotted in one color for simplicity.

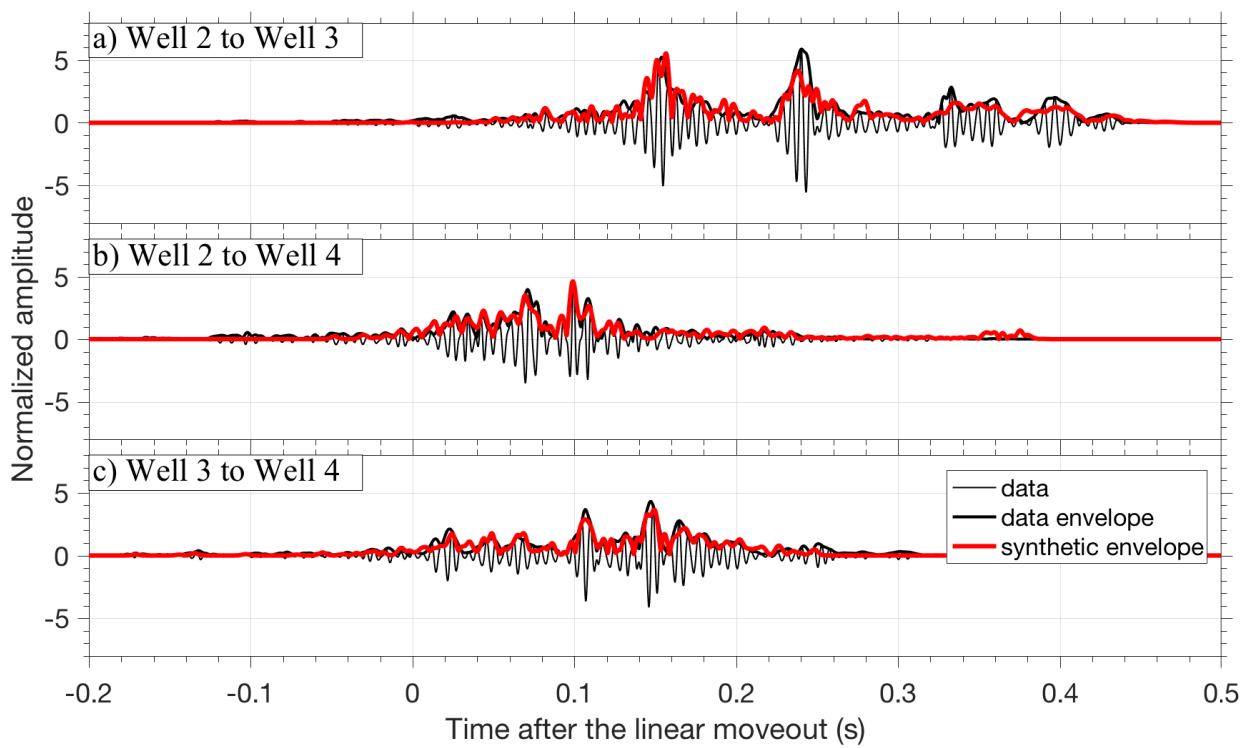


**Figure 11.** Comparison between observed and modeled envelopes of tube waves at each pair of wells. The tube waves are averaged over all sources and receivers after linear moveout correction (i.e., averaging waves shown in Figure 7 over sources and receivers) to increase the signal-to-noise ratio.

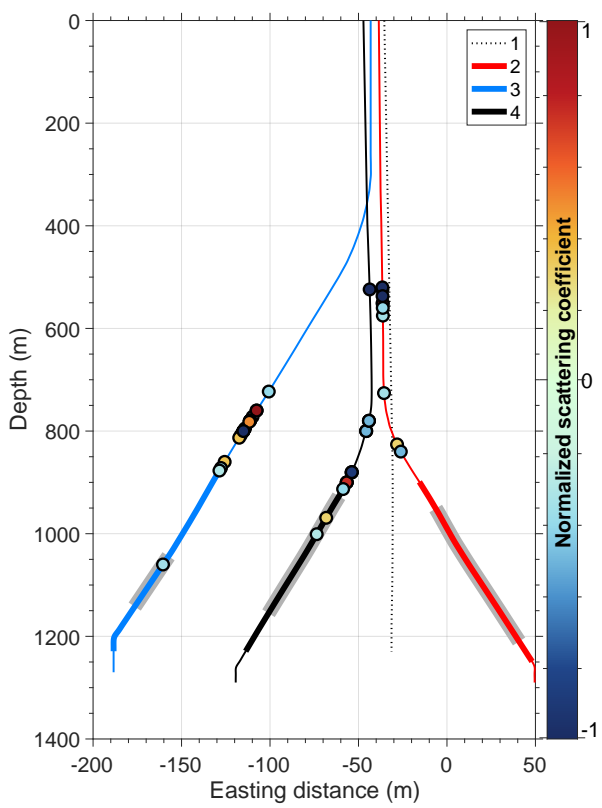


**Figure 12.** Locations of estimated scatterers and their relative scattering coefficient. The lines and color of wells are the same as them in Figure 1. Each circle shows the location of the scatterer and the color indicates the scattering coefficients. When the coefficient is negative, the polarity of the wave reversed after scattering.

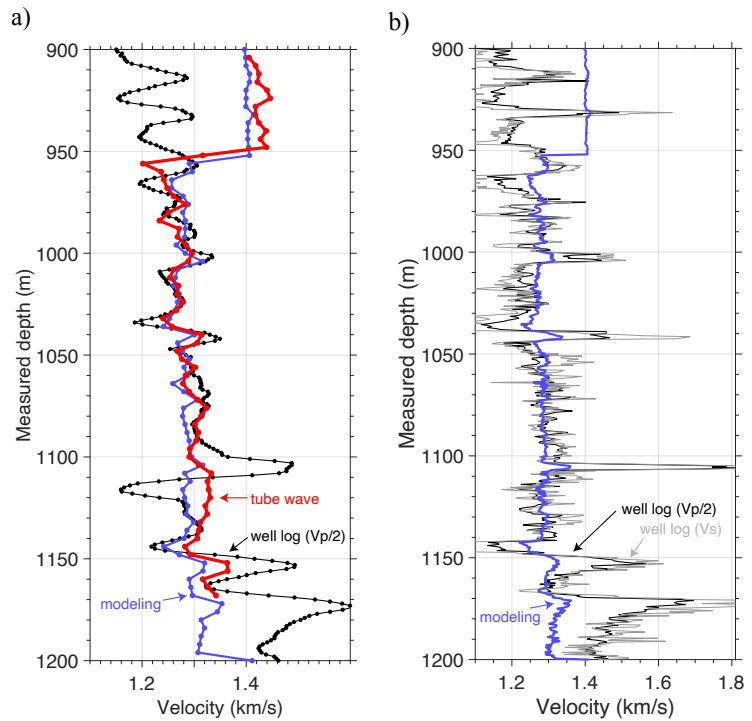


**Figure 13.** (a) Comparison of velocities measured by well logging (black), computed from the observed tube waves averaged over all available stages in Well 2 (red), and synthetic tube waves computed from the well-log data (blue). The velocities are estimated between sources. The well-log data (black) are downsampled to match the spatial sampling of those obtained by the tube-wave analysis. The reservoir of the injection is around 1110–1120 m in the measured depth. The well-log velocity is originally the P-velocity, and we assume that the ratio between  $V_p$  and tube-wave velocity is 2.0 to convert them. Casing materials change at 950 m depth from steel to FRP. The synthetic tube-wave velocities is estimated at 200 Hz. (b) Velocities of well logs and tube-wave modeling without spatial downsampling. Note that the well log data are at the baseline (i.e., before CO<sub>2</sub> injection) because S-wave velocity is only available at the baseline.

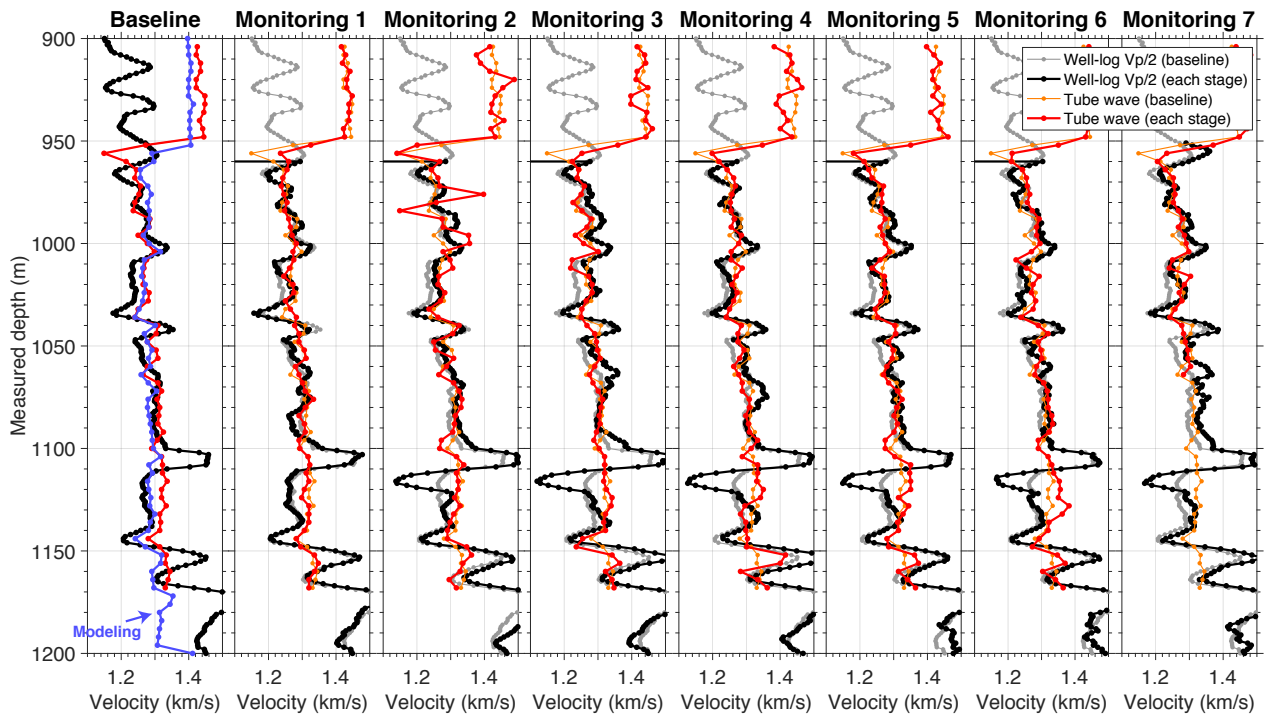


**Figure 14.** Same as Figure 13, but velocity estimation for all stages obtained without applying the source-location error correction at Well 2. The orange and gray lines are the copies of baseline curves.

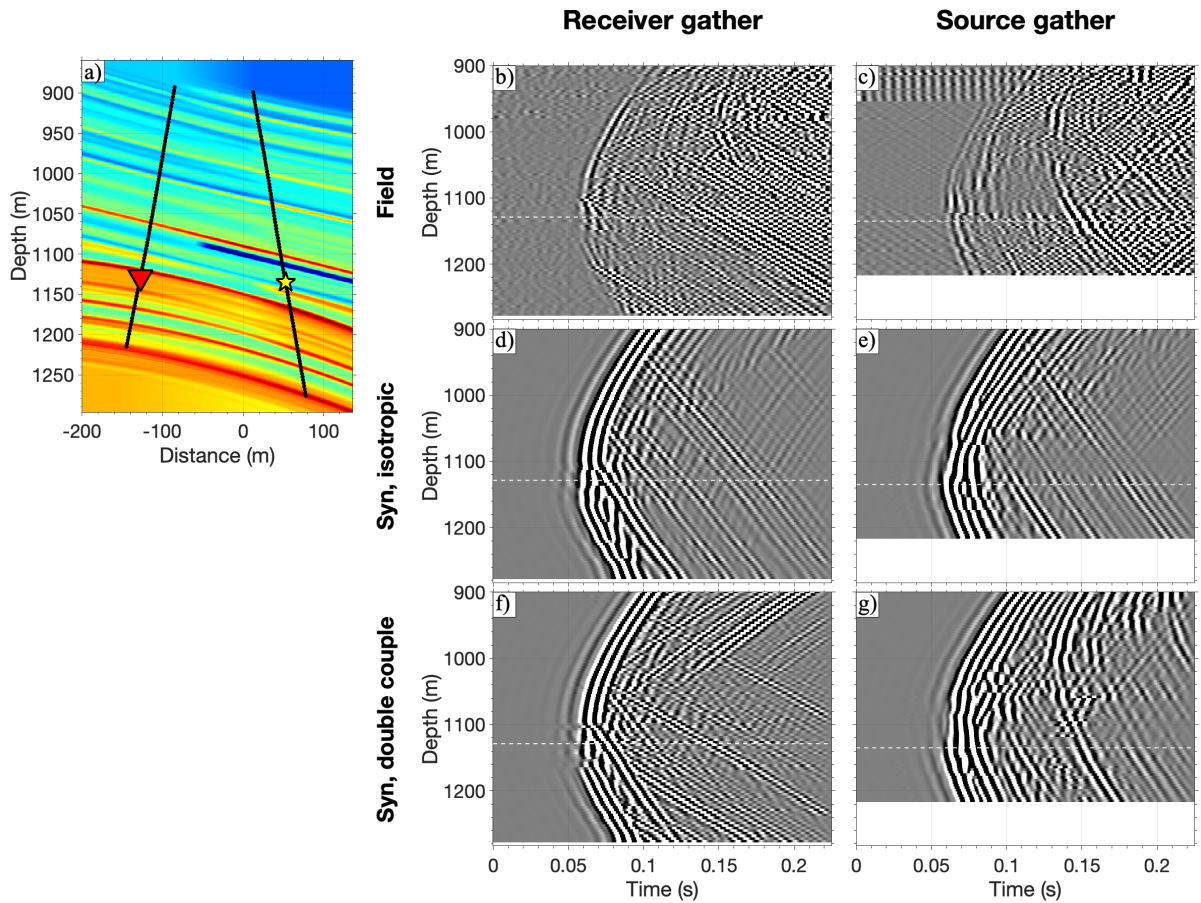


**Figure A1.** Comparison of field and synthetic data. (a) The locations of the source (yellow star) and receiver (red triangle) used for the source and receiver gathers, respectively. The background color shows the synthetic velocity model used for wavefield modeling. The source and receiver at 1140 m are shown as the star and triangle, respectively. (b,d,f) Source gathers and (c,e,g) receiver gathers. The three rows show gathers of the field data (b,c), synthetic data with an isotropic source (d,e), and synthetic data with a double-couple (dc) source (f,g). The nodal plane of the double-couple source is the horizontal direction. The white dashed line indicates the location of the common receiver or source locations.

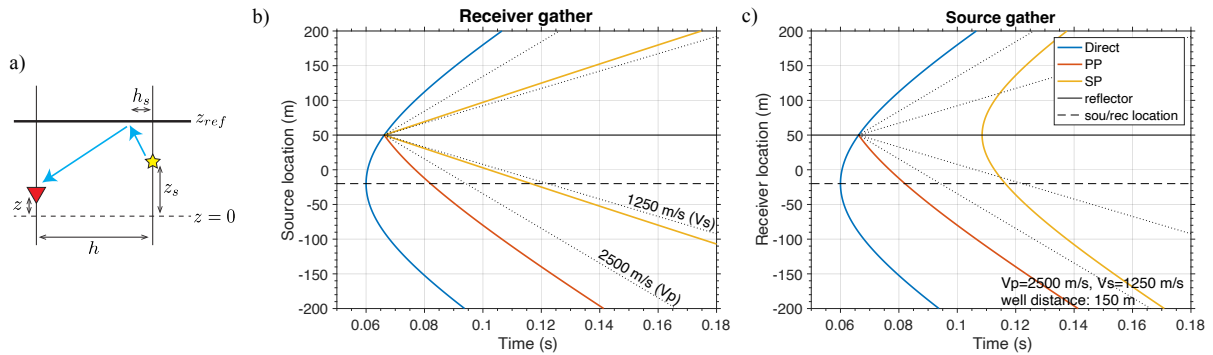


**Figure A2.** (a) Model of the analytical converted waves. The yellow star and red triangle show the location of source and receiver, respectively, and the horizontal thick black line is the location of the reflector. (b, c) Analytical travel times of direct P, PP, and SP converted waves for the receiver (b) and source (c) gathers when the reflector is at 50 m depth (solid black line). The common receiver and source are located at -20 m depth (dashed black line). The constant velocity and vertical wells are assumed for this analysis. The dotted lines indicate the velocity of 2500 m/s and 1250 m/s, respectively.